PHYSICAL REVIEW RESEARCH **7**, 023017 (2025)

Pattern formation in acoustically levitated particle systems with competing near-field interactions

Brady Wu,[*] Edward P. Esposito, Qinghao Mao, and Heinrich M. Jaeger
Department of Physics, University of Chicago, Chicago, Illinois, USA
and James Franck Institute, University of Chicago, Chicago, Illinois, USA

(Received 26 September 2024; accepted 7 March 2025; published 7 April 2025)

Acoustic levitation in air provides a containerless, gravity-free platform for investigating driven many-particle systems with nonconservative interactions and underdamped dynamics. In prior work the interactions among levitated particles were limited to attractive forces from scattered sound and repulsion from hydrodynamic microstreaming. We report on experiments in which contact cohesion provides a third type of interaction. When particle size and separation are both much smaller than the sound wavelength, this interplay of three interactions results in forces that are attractive over several particle diameters, become repulsive at close approach, and are again attractive at contact. In the presence of sound-induced athermal fluctuations that generate particle collisions, the interplay of these three forces enables the formation of particle chains with anisotropic interactions that depend on chain size and shape due to multibody effects. With the control of the kinetic pathways and the strength of the contact cohesion, different patterns can be assembled, from triangular lattices to labyrinthine patterns of chains to lacelike networks of interconnected rings. These results shed light on the multibody character of acoustic interactions and can be utilized to direct the self-assembly of particles.

DOI: 10.1103/PhysRevResearch.7.023017

I. INTRODUCTION

Objects in an acoustic field experience a force toward a sound pressure node or antinode, depending on the acoustic contrast with the surrounding medium [1]. This primary acoustic force acts on individual particles and has been utilized in a wide range of applications to levitate and manipulate particles [2,3]. In systems of multiple objects, the same acoustic field furthermore induces secondary forces that act between levitating particles [4]. One of these forces arises from scattered sound. In the near-field Rayleigh scattering regime, where the particles' size and separation are both much smaller than the sound wavelength λ, this leads to attractive interaction within the levitation plane [5]. For solid spheres of diameter D and center-to-center distance r the magnitude of this in-plane attraction scales as

$$F_{\mathrm{sc}}(r) \propto -\frac{E_0 D^6}{r^4}. \tag{1}$$

Here $E_0 = p_{\mathrm{ac}}^2/(2\rho_0 c^2)$ is the energy density resulting from sound pressure waves with amplitude p_{ac}, ρ_0 is the density of the embedding fluid medium (air or a liquid), and c is the speed of sound in that medium [5]. This force is shown by the blue curve in Fig. 1(a).

Another sound-induced secondary force arises from the finite viscosity of the embedding medium, which, as a result of the nonlinearity of the Navier-Stokes equations, leads to time-averaged net flow ("microstreaming") near solid particle surfaces. This microstreaming surrounds particles with a viscous boundary layer of characteristic thickness $\delta_\nu = \sqrt{2\nu/\omega}$, where ω is the sound frequency and ν is the kinematic viscosity [6], and it produces a repulsive in-plane force [Fig. 1(a), green curve] whose magnitude scales as [7]

$$F_{\mathrm{st}} \propto E_0 D^2 \exp[-(r-D)/\delta_\nu]. \tag{2}$$

For two levitating spheres the balance between scattering attraction and microstreaming repulsion establishes a stable steady-state separation [rightmost zero crossing of the black curve in Fig. 1(a)], which is controlled by the Stokes number $\Omega = \omega D^2/(4\nu) = 1/2(D/\delta_\nu)^2$. For $\Omega \approx 5$ two spheres have a steady-state separation of approximately one sphere diameter [6]. One can therefore independently tune the interaction strength through E_0 and the separation distance through Ω, i.e., via the sound frequency, particle size, or fluid viscosity. However, for identical spherical particles these attractive and repulsive forces both are isotropic within the levitation plane, which structurally limits the resulting assemblies to triangular configurations of either close-packed or slightly separated neighbors [7,8].

To go beyond triangular sphere configurations, acoustic levitation in air affords a special opportunity: The nonzero, but very small, viscosity of air makes it possible to enter a regime where collisions among particles can overcome the short-range repulsive forces and bring particles into direct contact. When this occurs, a third kind of interaction, contact cohesion, for example, due to van der Waals forces, can come into play [Fig. 1(a), orange curve].

---

[*] Contact author: bwu34@uchicago.edu

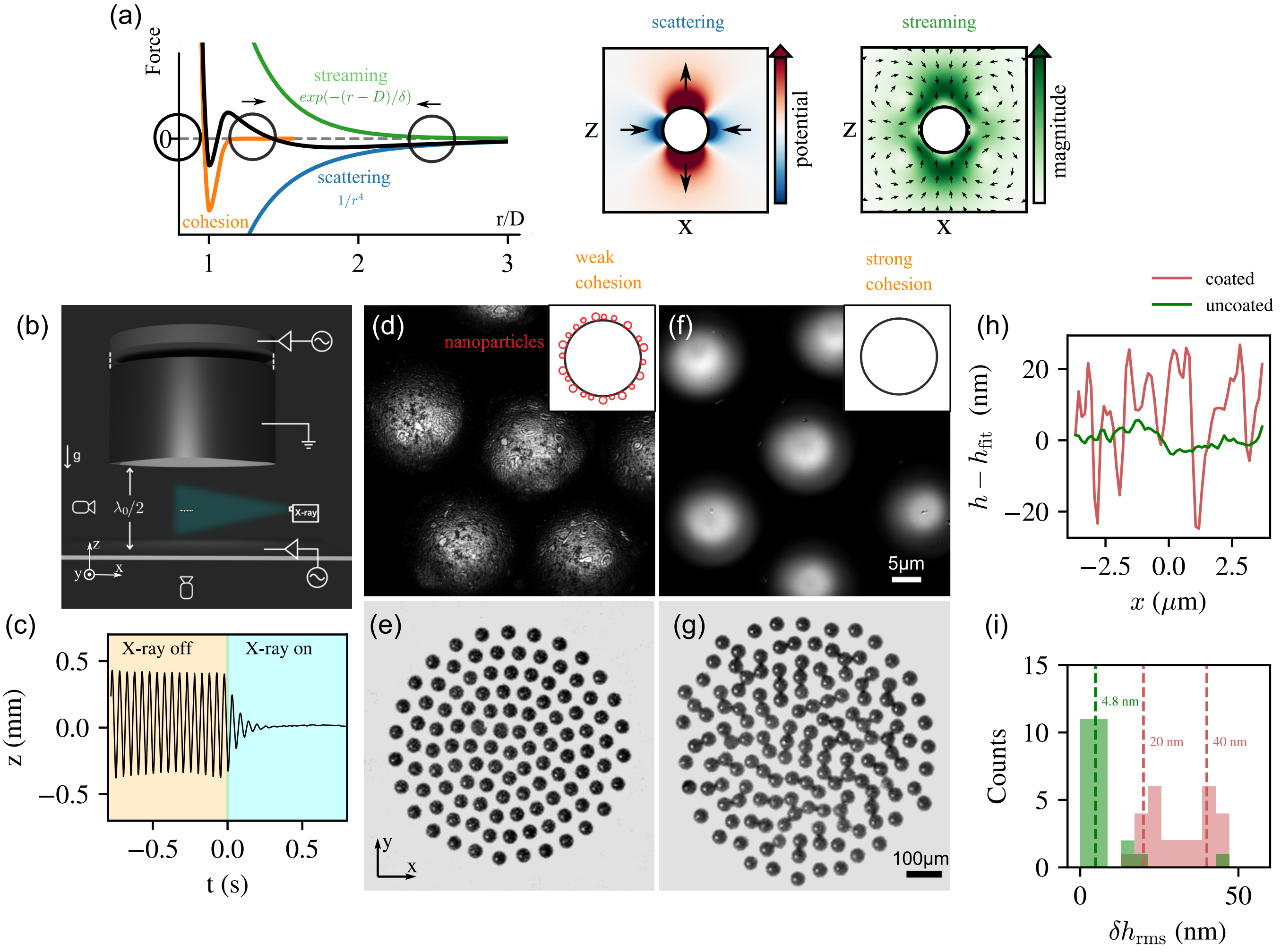

FIG. 1. Contact stickiness tuned by surface roughness. (a) Sketch of the types of forces present between a pair of spheres as a function of r/D, where r is their center-center separation and D is the particle diameter. Contact cohesion can bind two particles; the strength of the cohesive forces can be altered with surface roughness. Acoustic scattering and microstreaming are responsible for the in-plane attraction and repulsion, respectively. Together, they establish a stable sphere separation distance that is tunable by the Stokes number Ω. (b) Schematic of the experimental setup. A monolayer of particles levitates between a single-axis transducer and a transparent reflector. Charges on particles can be measured with an alternating electric field and neutralized by soft x rays. Particles are imaged from both the side and the bottom with high-speed cameras. (c) With charge on the particles present, a raft oscillates vertically under an electric field along the z direction. The oscillation decays within a fraction of a second once the x rays are turned on. Microscopy images of (d) and (e) Aerosil-coated particles and (f) and (g) uncoated particles, together with typical patterns they form when acoustically levitated. (h) Height profiles h along a line on the coated and uncoated particle surfaces. h_{fit} is a parabolic fit of the height profile. (i) Distribution of measured areal surface roughness δh_{rms}. The average rms roughness of coated particles is around 30 nm, significantly larger than that for uncoated particles.

This collision-enabled regime is reached in the limit of strong hydrodynamic coupling once the sound energy density E_0 becomes sufficiently large. The reason is that strong hydrodynamic coupling not only gives rise to repulsive microstreaming that separates pairs of particles (in experiments this occurs for $\Omega < 10$) but also induces hydrodynamic instabilities in many-particle systems [7]. Hydrodynamic instabilities can result from nonconservative forces generally and, here, from nonreciprocal forces (which are nonconservative by definition) more specifically. Microstreaming flows between two identical particles are symmetric and lead to reciprocal interactions, but in many-particle systems, asymmetries in the local particle configuration produce nonreciprocal streaming forces which can lead to spontaneously growing oscillations [9]. We believe that nonreciprocal microstreaming interactions are the dominant source of instabilities in this system, although scattering interactions have also been shown to be nonreciprocal [10,11]. These instabilities produce in-plane, athermal particle fluctuations around the particles' steady-state separation distance. Importantly, while the attractive and repulsive secondary acoustic forces in Eqs. (1) and (2) both increase linearly with E_0, the athermal fluctuations increase more strongly. This makes it possible, by simply increasing E_0 or, equivalently, the sound pressure, to inject kinetic energy so that random in-plane fluctuations drive collisions that lead to a finite probability for sticking when contact cohesion is present.

By controlling cohesion we can therefore establish a net force profile that is attractive at large particle separation, repulsive at short range (of order δ_ν), and attractive again at contact [Fig. 1(a), black curve]. Such profiles arise in colloids and vibrated grains interacting through electric or magnetic dipoles [12,13], as well as magnetic particles at a fluid interface [14]. The interactions have two stable positions and can therefore generate chain or ringlike structures and labyrinthine patterns. Here we investigate how this type of force profile leads to the formation and evolution of levitated particle chains in the presence of multibody interactions as well as athermal fluctuations.

We show that cohesion due to collisional contact can facilitate the formation of dimer particles, which then act as seeds for the formation of longer chain segments. We find that the chain-chain interactions are anisotropic and significantly less repulsive in the longitudinal (head-head) direction than in the transverse (side-side) direction. This anisotropy is chain size dependent, and longitudinal repulsion between chain heads weakens with increasing length, becoming entirely attractive when chains contain four or more particles. The anisotropic and size-dependent character is fundamentally due to the multibody nature of the interaction and cannot be recovered from any pairwise interaction models, in direct contrast to the above-mentioned studies [12–14]. Due to collisions and multibody interactions the chain segments connect and dissolve dynamically and also form occasional rings. Importantly, while in related thermal systems the interactions are pairwise and structural stability is determined solely by the local bond energy [15], here the stability is shape dependent, and we observe that rings have significantly longer lifespan than similarly sized chains. Taking advantage of the different stability of rings and chains, we then demonstrate that a levitated particle raft can be kinetically “quenched” to contain mostly linear chains or can be “annealed” to form a pattern of interconnected rings.

II. EXPERIMENTAL SETUP AND METHODS

Setup. Figure 1(b) sketches the experimental setup from the side. Particles are levitated in a horizontal $x-y$ plane, halfway along the vertical z axis in the center of the acoustic cavity formed by the gap between an ultrasound transducer (top) and a reflecting surface (bottom). The acoustic cavity is driven by a piezoelectric element onto which a frequency-tuned aluminum horn is bolted to amplify the acoustic power generation. The bottom of the metallic horn is concave with a radius of curvature $R = 50$ mm and is painted white to act as a light source for backlighting. The concave geometry weakly confines the particles near the central axis of the cavity. The horn temperature is regulated with a heater tape and a PID controller at $35\,^\circ\mathrm{C} \pm 0.5\,^\circ\mathrm{C}$ for experimental repeatability. The piezoelectric element is driven by applying a sinusoidal voltage V_{pp} in the range 60–200 V peak to peak at a frequency close to the resonance frequency of the horn, $\omega_0/(2\pi) = 34.870$ kHz. This signal is generated by a function generator and amplified by a high-voltage amplifier (A-301 HV amplifier, AA Lab Systems). The gap between the horn and reflector is adjusted to $\lambda_0/2$ by moving the horn with a motorized translation stage, where $\lambda_0 = 9.8$ mm is the wavelength associated with ω_0. Throughout all experiments, we keep the gap height constant. In order to minimize the effect of air currents, the entire setup is enclosed within an acrylic box with dimensions much larger than the levitation region ($L \times W \times H = 61 \times 30 \times 46\ \mathrm{cm}^3$).

Before and after each experiment, the bottom reflector is cleaned with deionized water and dried with compressed air. Particles are added to the cavity with tweezers. The reflector consists of a transparent glass plate so that levitating particles can be imaged from the side and below using two synchronized high-speed cameras. The reflector is coated with electrically conductive indium tin oxide. We neutralize residual charges on levitating particles *in situ* by applying soft x rays (Hamamatsu L12645 photoionizer) to the gap region for a few seconds, adopting a procedure introduced by Grosjean and Waitukaitis [16]. This method ionizes the surrounding air and eliminates surface charges of both polarities without introducing air flow. We can check for the presence of net charge by applying an oscillating electric field between the reflector and the metal horn to induce vertical oscillations of levitating particles or rafts [17]. The efficacy of removing net charge with soft x rays is seen in the rapidly decaying oscillation amplitude once the ionizer has been turned on (see Fig. 1(c) and also Movie S1 in the Supplemental Material [18]). After charge elimination, both the reflector plate and horn are grounded. In the experiments discussed in the following, particle motion occurs strictly within the levitation plane, and videos are recorded from below with a Vision Research Phantom T1340 camera at 3000 frames per second (fps), except for a few experiments operating at 20 000 fps where mentioned. The acoustic pressure near the edge of the cavity is measured with a laser-based sound sensor (Xarion Eta100 Ultra optical microphone). All experiments are performed, and particles are stored, within a humidity- and temperature-controlled laboratory environment (45%–50% relative humidity, $22\,^\circ\mathrm{C}$–$24\,^\circ\mathrm{C}$).

Particles. We use dry, spherical polystyrene spheres (microParticles GmbH, material density $\rho = 1000\ \mathrm{kg\,m^{-3}}$). These are highly size selected, with mean diameter $D = 41.11\ \mu\mathrm{m}$ and standard deviation $\sigma(D) = 0.5\ \mu\mathrm{m}$. Several forces could be responsible for cohesion between same-material, nominally dry particles. Once electrostatic forces due to residual charges on particle surfaces are eliminated, this leaves van der Waals forces and cohesion due to molecularly thin liquid films. With experiments under ambient conditions it is impossible to rule out bridges between contacting surfaces created by a few layers of liquid molecules. However, in both cases the magnitude of cohesion scales with the size of the contact area, and it rapidly diminishes with increasing surface roughness. The relevance of cohesion, and thus the shape of the force profile in Fig. 1(a), can therefore be controlled by roughening the particles, which we achieve by coating them with nanoparticles. A similar approach was previously found to suppress clustering in freely falling granular streams [19].

Figures 1(d)–1(g) show the difference in polystyrene particle surfaces and the resulting difference in the type of structure formed by the particles in a levitating raft when fumed silica nanoparticles of size less than $D/1000$ (Evonik, Aerosil 200, with ≈20 nm diameter primary silica particles) have been added. We measured the surfaces of coated and uncoated particles using an Olympus LEXT OLS-5000 laser-scanning confocal microscope. Figure 1(h) displays the difference between the height $h(x, y)$ and a parabolic fit h_{fit} along a line on the top of the spherical surface. The difference shows the typical surface roughness. The rms areal surface roughness is calculated from the measured surface height as $\delta h_{\mathrm{rms}} = \sqrt{\frac{1}{A}\iint_A [h(x,y) - h_{\mathrm{fit}}(x,y)]^2\, \mathrm{d}x\mathrm{d}y}$, where A is the surface area mapped for a particular particle. The histogram of δh_{rms} for the coated particles exhibits a bimodal distribution around its average, which indicates the roughness varies by about one primary particle diameter [Fig. 1(i)].

Notably, both coated and uncoated particles self-assemble into rafts with circular boundaries [Figs. 1(e) and 1(g)]. In our experiments, this self-assembly is not caused by a steep potential well that confines the particles and drives them to self-arrange within a fixed circular area. The primary, single-particle confining forces in the $x-y$ levitation plane fix the raft at the center of the cavity but are much weaker than the interparticle interaction and do not contribute to the circular boundary. The outer edge is circular due to an effective surface tension that arises from multibody interactions and minimizes the surface [20]. The size of the rafts will simply grow with additional particles while keeping the boundary circular. As the center particles self-organize into a triangular lattice, 5-fold and 7-fold coordinated defects exist to mediate the transition between crystalline core and circular boundary in rafts of coated particles.

Analysis of levitated particles. Particle positions are obtained from a custom tracking algorithm, which utilizes the WATERSHED algorithm to separate particles in contact, followed by the REGIONPROPS algorithm to obtain the centroid of individual particles (performed using module SKIMAGE version 0.22.0 implemented in PYTHON version 3.9.12). After positions are obtained for all particles at each frame, trajectories are linked with TRACKPY (version 0.6.1). Before analysis, any global translation and rotation of the rafts (typically negligible) are subtracted from the xy positions of individual particles. The velocity of particle i at time t is calculated as $v_i(t) = |\vec{r}_i(t) - \vec{r}_i(t - \Delta t)|/\Delta t$, where $\vec{r}_i(t) = (x, y)$ is the position of particle i at time t and $\Delta t = 0.33$ ms. We classify two particles as bonded if $r/D < 1.05$. We identify rings by looking for the enclosed empty spaces in the rings in each frame.

Simulations. To perform finite-element simulations of particles interacting in the acoustic cavity we use COMSOL MULTIPHYSICS software. Solutions are obtained by first solving the linearized Navier-Stokes equation utilizing the Thermoviscous Acoustics, Frequency Domain module. This method considers viscous effects and properly resolves the acoustic boundary layer. Next, the second-order time-averaged net flow is solved by adding the necessary source terms (from the first-order solution) to the Laminar Flow interface [21]. The solution obtained is the steady-state time-averaged solution at long times and is free from any transients. Particles are simulated in a rectangular box of height $10D$ and width $40D$. The top and bottom walls are actuated in phase with a fixed displacement amplitude and driving frequency that mimic the experiment. The side walls of the simulation box have periodic boundary conditions to avoid reflections and other finite-size effects. The minimal and maximal mesh sizes used around a particle are 0.6 and 9.5 μm, respectively, to resolve viscous and streaming effects appropriately.

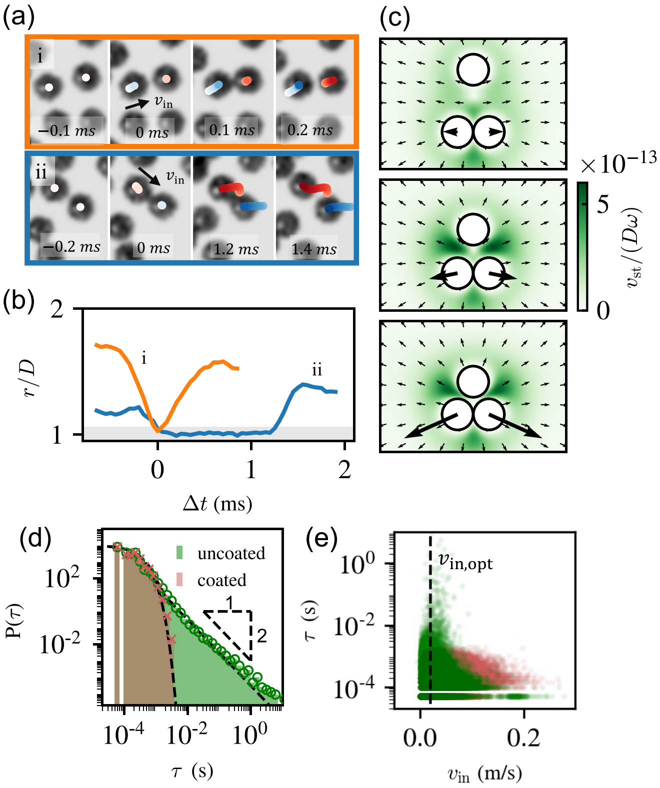

FIG. 2. Dimer formation due to contact adhesion. (a) Examples of two particles colliding with impact velocities $v_{\mathrm{in}} = 0.035$ m/s [diagram (i)] and $v_{\mathrm{in}} = 0.06$ m/s [diagram (ii)]. (b) The relative separations r/D between the two particles in (a). Particles are classified as in contact for $r/D < 1.05$ (gray region). (c) Numerical simulations of time-averaged microstreaming flow around the dimer as a third, intruding particle approaches. Arrows denote forces on dimer particles. (d) Distribution of the bond lifetime τ for dimers. The black dashed line for the coated particles represents an exponential distribution. (e) Dimer bond lifetime τ as a function of relative impact speed v_{in}.

III. RESULTS AND DISCUSSION

Strong hydrodynamic coupling is achieved when particles are no more than one to two viscous boundary layer thicknesses apart but also are not contacting already in the steady state without collisions (as that would lead to frictional contact and suppress fluctuations). This requires Stokes numbers $\Omega \leqslant 10$ [7]. For levitation in air at frequencies around 40 kHz, where $\delta_\nu \approx 10$ μm, it therefore requires particle sizes $D \leqslant 50$ μm. We first discuss the formation of the smallest anisotropic objects, dimers of two spheres that have stuck together and "bonded." We then show how the resulting anisotropic interactions of dimers with other particles lead to chain and ring formation. Finally, we demonstrate how the different lifetimes of chains and rings make it possible to guide the assembly of particles in the levitation plane into different overall patterns by selecting kinetic pathways.

A. Collisions and formation of dimers

Figure 2(a) illustrates instances where two particles overcome the streaming repulsion, collide with impact velocity v_{in}, and rebound [diagram (i)] or "stick" [diagram (ii)]. At contact and under mechanical equilibrium, attraction from cohesion and acoustic scattering balances with repulsion due to acoustic streaming and elastic deformation of the colliding particles. The strength of the resulting bond between the particles then depends on surface roughness and impact velocity. We employ high-speed imaging at 20 000 fps and particle tracking with a resolution of 1 μm to track the impact process and determine the impact velocity. Figure 2(b) presents the interparticle distance as a function of time for the two examples in Fig. 2(a). We classify two particles as "in contact" for $r/D < 1.05$, which is denoted by the gray area.

Fluctuations in particle position not only enable collisions and the formation of bonds but also can modulate the strength of existing bonds and thus lead to a finite bond lifetime. This is shown by the simulation in Fig. 2(c), which illustrates the streaming flow field and the net acoustic forces on a preexisting dimer comprising two spheres when a third sphere approaches in the xy levitation plane. When the third sphere is sufficiently far away, the mutually repulsive interaction of the dimer particles from microstreaming is small. However, at closer approach and well before any contact, the third particle drastically intensifies the intradimer repulsion, potentially overcoming the contact cohesion and breaking the bond that holds the dimer together.

Generally, for a time-independent decay process, the survival time of a bond, once formed, is expected to follow $\exp(-\tau/\tau_0)$, where τ_0 is a characteristic bond lifetime. When there is a distribution of lifetimes $P(\tau_0)$, the distribution of survival times becomes $P(\tau) = \int_0^\infty \exp(-\tau/\tau_0)P(\tau_0)\,d\tau_0$. Figure 2(d) shows $P(\tau)$ for dimers as obtained from the experiments (data for chains of more than two particles follow similar distributions; see Fig. S1 and the Supplemental Material for details). For the coated particles, $P(\tau)$ is shown in red and follows an exponential distribution, with τ_0 around 0.2 ms, over more than 5 orders of magnitude. This is also reflected in the peak near 0.2 ms when we plot how τ depends on relative collision impact velocity v_{in} [red data in Fig. 2(e)].

The bond lifetime of uncoated particles decays much slower at long time and close to the power law $P(\tau) \propto 1/\tau^{\alpha}$, with exponent $\alpha \approx 2$ [green portion of the histogram in Fig. 2(d)]. Such a power law tail for $P(\tau)$ indicates an associated power law distribution of characteristic lifetimes, $P(\tau_0) \propto 1/\tau_0^{\alpha+1}$. The overall distribution of bond survival times $P(\tau)$ can then be well reproduced by a lifetime distribution $P(\tau_0)$ that combines a Gaussian with a power law (dashed line; see Fig. S2 and the Supplemental Material for details).

One condition for forming a long-lasting bond is that there is no immediate rebound after a collision. From Fig. 2(e) we see that bonds with long survival times form only for uncoated particles and for impact velocities $v_{\text{in}} < 0.05$ m/s. We can estimate the optimal impact velocity at which the elastic deformation due to impact balances with the surface adhesion energy, arriving at $v_{\text{in,opt}} \approx 0.02$ m/s (black dashed line; for details see the Supplemental Material), near the experimentally observed peak in the survival times.

As the relative impact speed increases beyond $v_{\text{in,opt}}$, the survival times systematically decrease because the elastic energy provided by the rebound becomes sufficient to weaken and eventually overcome the adhesion energy. At the largest impact speeds, around $v_{\text{in}} = 0.2$ m/s, uncoated particles detach immediately after a collision, while coated particles can still form dimers that survive for a few milliseconds. This suggests that coated particles can more efficiently absorb incoming kinetic energy, possibly due to impact-induced rearrangements within the one to two layers of nanoparticles on their surfaces.

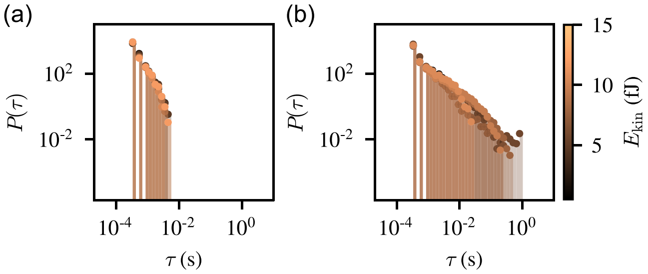

FIG. 3. Particle kinetic energy does not affect bond lifetime. Distributions $P(\tau)$ of bond lifetimes τ for a range of different kinetic energies, averaged over 1 s, plotted separately for (a) coated and (b) uncoated particles.

In a thermally driven system, we would expect $\tau_0 \propto \exp(E_{\text{b}}/k_BT)$, where E_{b} is the bond energy and k_BT is the energy associated with thermal fluctuations. Thus, $P(\tau)$ would depend on temperature. However, the fluctuations here are athermal. If we take the kinetic energy E_{kin}, time averaged over all particles, as the measure of an effective temperature, we find that the distribution of lifetimes $P(\tau)$ is independent of E_{kin} for both the coated and uncoated particles [Figs. 3(a) and 3(b)]. Therefore, τ_0 cannot be directly related to E_{b} in this system.

B. Anisotropic interactions lead to chain and ring formation

The presence of dimers, especially long-lived ones, introduces anisotropic interactions with other objects in a levitating raft. This is seen most directly from finite-element simulation of the net force between two chains of different length [Fig. 4(a)]. In these plots, two chains are aligned head-to-head in the longitudinal direction unless specified otherwise, and r is the center-to-center spacing between the particles forming the two heads. Interchain repulsion weakens significantly for chains of increasing length, reducing the stable separation r_{st} given by the zero crossing of the force curve. This size dependence of the chain-chain interaction directly demonstrates the consequence of high-order multibody interactions that go beyond three spheres.

Interestingly, the interaction becomes entirely attractive between two chains of four particles each $(4 + 4)$, suggesting that sufficiently long chain segments will link up spontaneously. However, two chains arranged side by side always experience significant repulsion, and their stable transverse separation is larger than head-to-head (purple curve). Figure 4(b) shows how this is due to increased microstreaming in the direction transverse to a short chain, here comprising three spheres. Similar anisotropic interaction arises for capillary forces between two rods at a two-fluid interface [22], both leading to preferential end-to-end bonding.

The presence of dimers and short chain segments therefore serves to seed the growth into longer chains since the

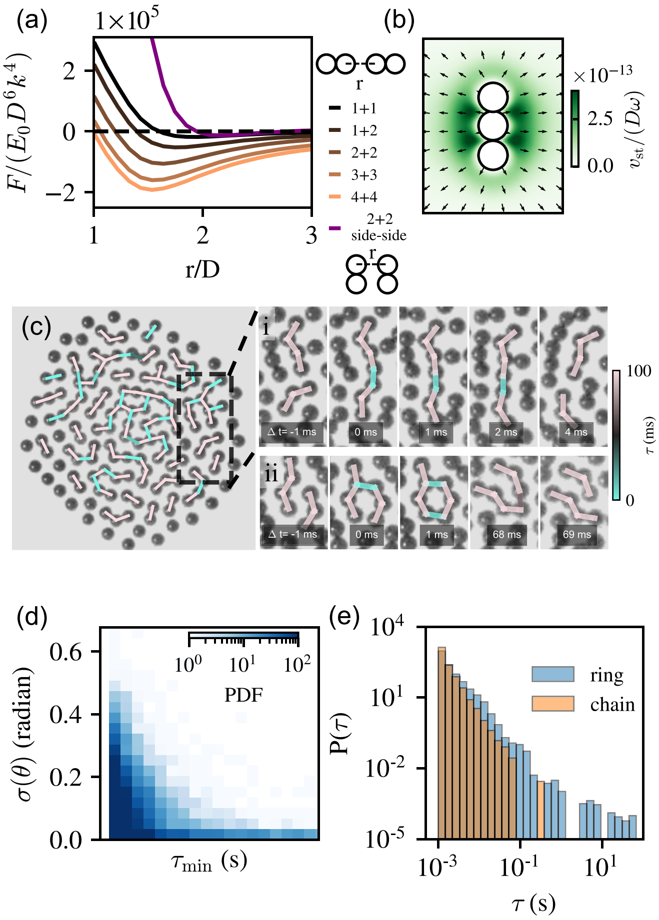

FIG. 4. Bond formation and the dynamics of chains and rings. (a) The net force between two chains of different length as obtained from finite-element simulations. The legend specifies the number of particles in each chain. The chains are in the longitudinal (head-head) configuration, unless otherwise noted. (b) The streaming flow in the xy plane around a chain of three particles, obtained from finite-element simulations. (c) Bottom view of a raft of uncoated particles. Bonds are colored by their lifetime. Diagrams (i) and (ii) show the formation and breakdown of a chain and a ring. (d) PDF of the standard deviation of the angles $\sigma(\theta)$ as a function of the minimum lifetime $\tau_{\rm min}$ between any two bonds. (e) PDF of the lifetime of the ring and chain structures. Most of the chain structure breaks down within 0.1 s after formation.

anisotropic interactions lower the energetic cost of collisions along the longitudinal, head-to-head direction. We note that the magnitude of repulsion has little effect on the bond survival time (Fig. S1), indicating that contact cohesion is the dominant factor for bond strength. The anisotropic interaction is qualitatively similar for a wide range of Stokes number Ω (see Fig. S3 and the Supplemental Material for details).

In the experiments, fluctuations induced by hydrodynamic coupling let chains collide with other chains or single particles, thereby establishing transiently connected structures that are stabilized by cohesive bonds with different survival times τ. An example is shown in Fig. 4(c) (see also Movie S2). Generally, at any given instant nearly half the bonds are long-lived [colored pink in Fig. 4(c)] and stabilized by strong cohesion and/or the specific configuration of neighboring particles, such as rings (see below). These bonds therefore rarely break. The other half (colored cyan) are held together by weak cohesion or anisotropic acoustic attraction, usually breaking within a few milliseconds after formation. In Fig. 4(c), diagram (i) shows a representative example of two chain segments first connecting in the longitudinal direction and then disconnecting. Bonds can be flexible, seen here by the changing angle between cyan and pink bonds.

Occasionally, two neighboring chains form a ringlike structure [Fig. 4(c), diagram (ii)]. To form a ring, the two approaching chains are usually bent. In this particular case, the two new bonds leading to the ring form sequentially, which is possible because of the flexibility of short-lived bonds. To quantify this behavior, we extract from the experimental data the standard deviation $\sigma(\theta)$ of the angle θ between any two neighboring bonds. Short-lived bonds tend to be more flexible and have larger $\sigma(\theta)$ due to the lower energy cost of rolling, and they usually break quickly unless the two chains form a more stable structure such as a ring [Fig. 4(d)].

Figure 4(e) quantifies the survival time distributions of rings and chains, here counting only rings and chains of similar sizes (five to seven particles). While these two types of structures have a similar distribution up to 0.1s, rings can survive over multiple seconds, outlasting chains by more than an order of magnitude in time.

This geometry-enhanced longevity of the rings may come as a surprise in comparison to thermal systems, where the structural lifetime depends solely on their energy levels, and thus, the lifetimes of the rings and chains are expected to follow the same distribution as long as their energy levels are the same. However, the fluctuations here are athermal, as evidenced by the nonexponential distribution of the structural lifetimes. Fluctuating particle positions in our system can generate a weakening of existing bonds [see Fig. 2(c)]. While chains are exposed to fluctuations on both sides, closed rings are susceptible on only one side. Additionally, forces generated by an approaching external particle similar to the one in Fig. 2(c) naturally conform more closely to the curved geometry of a ring than to a linear chain; thus, a closed ring can resist such forces better, which enhances its stability. Finally, the rms velocity of air at the center of the ring is over 50% larger than the air velocity around a chain (Fig. S4), which could stabilize the rings. This dependence of the local air velocity on the specific particle configuration again shows the necessity to consider high-order multibody interactions.

The stability of rings has another implication: When multiple rings interconnect, the resulting lacelike structure (especially the interior) will experience fewer fluctuations than regions filled with linear chain segments. We next illustrate how to leverage this difference in lifetimes to control the formation of distinct structures.

C. Kinetic pathways control structure formation

As the acoustic pressure $p_{\rm ac}$ is increased, and with it the sound energy density $E_0 \propto p_{\rm ac}^2$, in-plane particle fluctuations due to hydrodynamic coupling become significant and lead to an increase in the particles' kinetic energy [7]. Figure 5(a) shows this pressure dependence of the kinetic energy $E_{\rm kin}$ in the levitation plane, averaged over all N particles in the raft

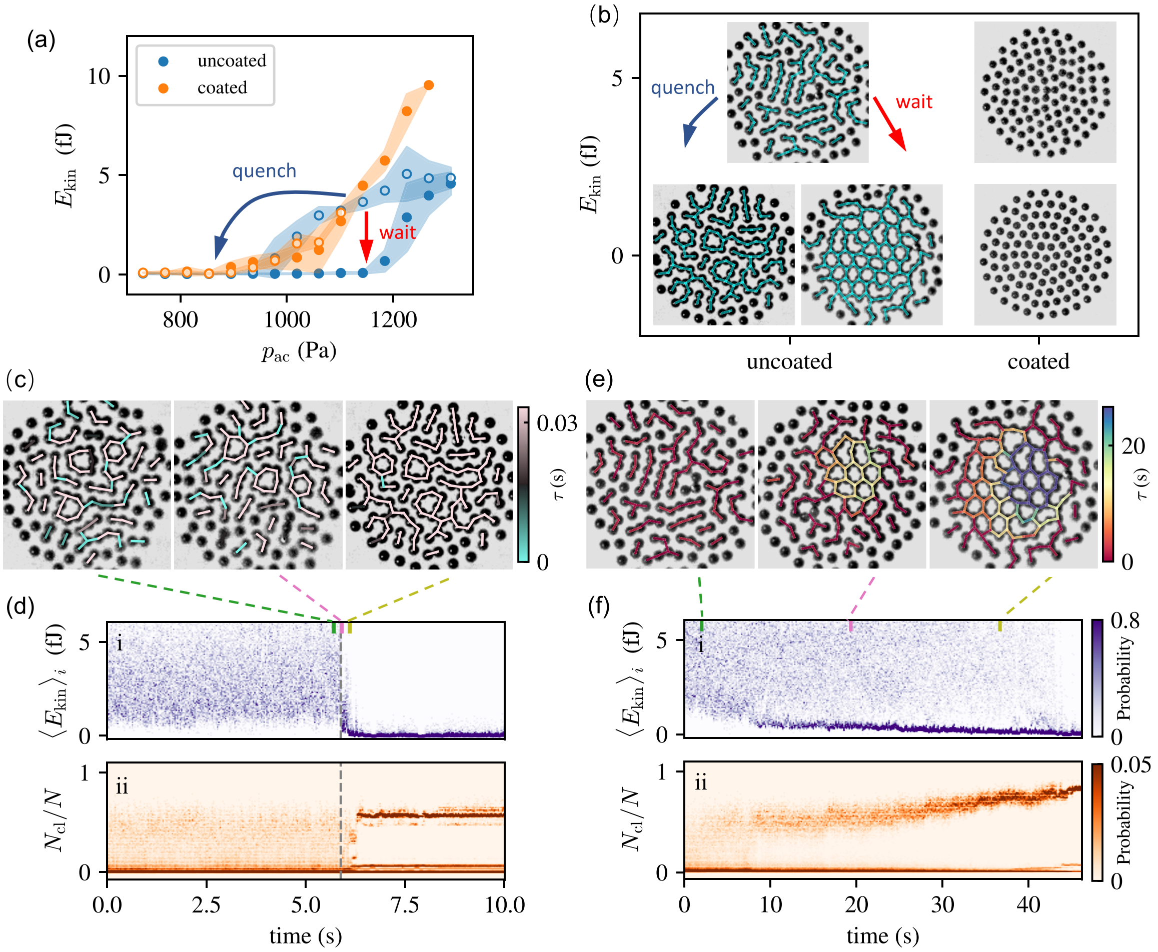

FIG. 5. Kinetic pathway controls structural formation. (a) Kinetic energy $E_{\rm kin}$ as a function of acoustic pressure $p_{\rm ac}$ for coated and uncoated particles, time averaged over 1 s. Solid and open symbols represent increasing and decreasing $p_{\rm ac}$, respectively. Blue and red arrows show two pathways of structural formation. (b) At high $E_{\rm kin}$, a raft of uncoated particles contains relatively short branches. By quenching the system (i.e., from high to low $p_{\rm ac}$), a raft of mostly linear branches forms, whereas annealing produces a raft with interconnected rings. Coated particles do not form any connected structure at high or low $E_{\rm kin}$. Experimental snapshots of the raft during (c) quenching and (e) annealing. (d) and (f) Measured distribution of the single-particle kinetic energy $\langle E_{\rm kin}\rangle_i$ [diagram (i)] and the size of cluster of connected particles N_{cl} normalized over all particles N [diagram (ii)] during quenching and annealing process. The time resolution of the distributions is 0.15 s.

for 1 s, which provides a measure of the effective temperature in the system. Notably, unlike rafts of coated particles, rafts comprising uncoated particles exhibit a hysteresis when the acoustic pressure is cycled. This hysteresis results from particle chains and rings that can grow into interconnected, system-spanning structures. If cohesion is present, a small number dimers can act as seeds for longer chain segments that eventually grow into branching structures of interconnected chains and rings as they link up with individual particles or neighboring segments. These connected structures have a finite rigidity and are capable of suppressing hydrodynamic instabilities which require degrees of freedom in particles' motions to extract energy. To disrupt these structures, acoustic pressure needs to be increased until the acoustic forces overcome cohesive bonds and the connected structures are broken apart.

Five categories of distinct structural patterns can be obtained by adjusting the strength of the fluctuations and the contact cohesion [Fig. 5(b); see also Fig. S5]. Due to the hysteresis, there can be two kinetic pathways for obtaining system-spanning connected structures. They are illustrated by the blue and red arrows in Figs. 5(a) and 5(b). The blue arrow denotes "quenching," where the acoustic pressure is instantaneously changed from high to low. The resulting pattern is composed mostly of linear chain segments. The red arrow denotes "waiting," where the acoustic pressure remains constant. In this case, due to the higher stability of the rings the system anneals over time: an island of interconnected rings forms and grows radially outward by absorbing chain segments. Eventually, linear chains attach to the edge of the ring aggregate, limiting the motion of even the isolated particles.

How kinetic pathways direct structure formation here is, in spirit, similar to quenching and annealing in thermal systems. In two-dimensional colloidal systems, for example, a quenched structure tends to be more disordered and glassy, usually polycrystalline with many grain boundaries, while annealing will produce more ordered crystalline regions with fewer defects [23,24]. Generally, a quenched structure, under enough fluctuations, will naturally evolve toward an annealed structure, which has a lower global energy. In contrast, here neither structure will spontaneously evolve toward the other. To transition between ring and chain structures, one would need to first increase acoustic pressure and break down the current structure to generate individual small chains and then use quenching or waiting to produce the targeted structure.

Figure 5(c) shows snapshots of a raft before, during, and after quenching, with bonds colored by their survival time. Before quenching, the system is in a statistical steady state, with linear chains, occasionally some rings, and individual particles. New bonds continuously form and break, but once quenched, the system falls into a local energy minimum and remains in a kinetically trapped state (see Movie S3). This evolution can be visualized by plotting, as a function of time, the distribution of time-averaged kinetic energy $\langle E_{\text{kin}} \rangle_i$ for each particle i [Fig. 5(d), diagram (i)] together with the number of particles in a connected cluster N_{cl} normalized by the total number of particles N [Fig. 5(d), diagram (ii)].

If instead p_{ac} is simply kept constant (blue arrow), the stability of the rings drives the accumulation of lacelike structures, whereby rings aggregate to form a small "island"' and eventually percolate [Fig. 5(e)]. This process has a distinct kinetic energy distribution and associated growth process [Fig. 5(f)]. Starting again from a steady state with large kinetic energy and a fluctuating, statistical distribution of chain segments, the formation of a ring seeds further ring formation. The larger stability of rings effectively lowers the local kinetic energy, thus also stabilizing any new bonds with chains that attach (Movie S4). The concentration of low $\langle E_{\text{kin}} \rangle_i$ starting near 10 s demonstrates this local suppression of fluctuations and indicates the formation and growth of ring structures. In Fig. 5(e) the lacelike structure of interconnected rings expands over time, as seen by the increasing number of particles in the cluster N_{cl}. This growth stops once the interconnected rings account for over 80% of the particles in the raft and the chain segments that protrude radially outward start to constrain the movement of the single particles remaining near the edge of the levitating raft.

IV. CONCLUSIONS

This work explored the self-assembly of mesoscopic structures in an athermal system, where fluctuations are driven by the inherent hydrodynamic instabilities in acoustic interactions, which are controllable via the sound intensity. We showed how the particle configuration in an acoustically levitated raft of small spheres can be tuned from a triangular lattice to an aggregate of linear chains or interconnected rings via different kinetic pathways. This tunability exploits the emergence of anisotropy in the sound-induced interactions when spheres bind due to cohesion and form dimers that act as seeds for highly flexible chains, and it relies on rings having a much longer lifetime than similarly sized chain structures. This is similar to the colloidal kagome lattice made of surface-coated "triblock Janus" particles [25], where the rings are designed to be the lowest energy state, but here it is possible thanks to the athermal nature of the fluctuations.

In many-particle systems labyrinthine patterns can generally arise in the presence of three competing forces: a short-range attraction, an intermediate-range repulsion, and a long-range attraction. Experimentally, this can be realized in monolayers of particles with field-induced electric or magnetic dipoles, as demonstrated by Dong *et al.* [12] and Merminod *et al.* [13]. Near contact, dipoles can attract if the particles are slightly misaligned, but they repel at a longer distance. Dong *et al.* and Merminod *et al.* then imposed external confinement using either acoustic forces or hard walls, which is equivalent to a long-range attraction, thereby producing the labyrinthine patterns. For induced dipoles, both short-range attraction and intermediate-range repulsion scale with dipole strength in the above systems. Here we were able to independently vary the relative strength of all three interactions through the surface coating and the Stokes number. Therefore, one could potentially utilize acoustic levitation to produce diverse labyrinthine patterns with different spacing between the chains.

The chain structures resulting from pairwise interactions are usually short, consisting of fewer than 10 particles [12,13], and a large system-spanning cluster will not form unless strong external confinement is imposed. In contrast, here we found that chains will spontaneously form system-spanning branching structures during quenching without any external confinement. As the interchain forces become less repulsive and eventually become attractive with a growing number of particles, the system naturally favors large connected structures. This result exemplifies multibody interaction as an additional useful knob for engineering self-assembled structures.

Due to the presence of an effective surface tension, the spatial distribution of particles and connected clusters naturally evolves to minimize the length of the raft boundary. The shape of this boundary is therefore always circular. Additionally, as the larger particles have smaller stable separations, it is more spatially efficient to have them in the raft center, where they have more neighbors [7]. Therefore, the rings and chains tend to aggregate at the center of the raft, leaving the single particles near the edge (Fig. S6). The concentration of ring and chain structures in the core facilitates the formation of one interconnected, system-spanning lacelike structure during annealing. As single particles exhibit the strongest repulsion when approaching other clusters [Fig. S3(b)], they rarely participate during the quenching and annealing process and are usually left near the outer raft edge.

The spontaneous aggregation during quenching is driven by acoustic attraction, but further work is needed to ascertain whether the resulting structure is stabilized by the acoustic interaction or by contact adhesion. In our current experiments it is difficult to disentangle these two types of attraction for chains composed of more than three particles. Rafts containing only a few chains are typically found to be incapable of growing a system-spanning cluster. It is also not yet clear what fraction of chains and average chain length are needed for the spontaneous aggregation of chains observed during quenching since under the conditions discussed here the chains form via random collisions, which results in a range of lengths from two to five particles. To resolve these questions, future experiments could use three-dimensional fabricated chains of controlled length and test the role of contact adhesion between chains by minimizing it by coating particle surfaces with nanoparticles.

ACKNOWLEDGMENTS

This research was supported by the National Science Foundation through Award No. DMR-2104733. The work utilized the shared experimental facilities at the University of Chicago MRSEC, which is funded by the National Science Foundation under Award No. DMR-2011854. The research also benefited from computational resources and services supported by the Research Computing Center at the University of Chicago.

---

[1] H. Bruus, Acoustofluidics 7: The acoustic radiation force on small particles, Lab Chip **12**, 1014 (2012).

[2] A. Ozcelik, J. Rufo, F. Guo, Y. Gu, P. Li, J. Lata, and T. J. Huang, Acoustic tweezers for the life sciences, Nat. Methods **15**, 1021 (2018).

[3] A. Marzo, S. A. Seah, B. W. Drinkwater, D. R. Sahoo, B. Long, and S. Subramanian, Holographic acoustic elements for manipulation of levitated objects, Nat. Commun. **6**, 8661 (2015).

[4] M. X. Lim, B. VanSaders, and H. M. Jaeger, Acoustic manipulation of multi-body structures and dynamics, Rep. Prog. Phys. **87**, 064601 (2024).

[5] G. T. Silva and H. Bruus, Acoustic interaction forces between small particles in an ideal fluid, Phys. Rev. E **90**, 063007 (2014).

[6] D. Fabre, J. Jalal, J. S. Leontini, and R. Manasseh, Acoustic streaming and the induced forces between two spheres, J. Fluid Mech. **810**, 378 (2017).

[7] B. Wu, B. VanSaders, M. X. Lim, and H. M. Jaeger, Hydrodynamic coupling melts acoustically levitated crystalline rafts, Proc. Natl. Acad. Sci. USA **120**, e2301625120 (2023).

[8] M. X. Lim, A. Souslov, V. Vitelli, and H. M. Jaeger, Cluster formation by acoustic forces and active fluctuations in levitated granular matter, Nat. Phys. **15**, 460 (2019).

[9] T. Beatus, T. Tlusty, and R. Bar-Ziv, Phonons in a one-dimensional microfluidic crystal, Nat. Phys. **2**, 743 (2006).

[10] N. St. Clair, D. Davenport, A. D. Kim, and D. Kleckner, Dynamics of acoustically bound particles, Phys. Rev. Res. **5**, 013051 (2023).

[11] E. M. King, M. C. Morrell, J. B. Sustiel, M. Gronert, H. Pastor, and D. G. Grier, Scattered waves fuel emergent activity, Phys. Rev. Res. **7**, 013055 (2025).

[12] R.-Y. Dong, W. Wang, and S. Granick, Colloidal flatlands confronted with urge for the third dimension, ACS Nano **13**, 9442 (2019).

[13] S. Merminod, T. Jamin, E. Falcon, and M. Berhanu, Transition to a labyrinthine phase in a driven granular medium, Phys. Rev. E **92**, 062205 (2015).

[14] A. Hooshanginejad, J.-W. Barotta, V. Spradlin, G. Pucci, R. Hunt, and D. M. Harris, Interactions and pattern formation in a macroscopic magnetocapillary SALR system of mermaid cereal, Nat. Commun. **15**, 5466 (2024).

[15] R. W. Perry, M. C. Holmes-Cerfon, M. P. Brenner, and V. N. Manoharan, Two-dimensional clusters of colloidal spheres: Ground states, excited states, and structural rearrangements, Phys. Rev. Lett. **114**, 228301 (2015).

[16] G. Grosjean and S. Waitukaitis, Single-collision statistics reveal a global mechanism driven by sample history for contact electrification in granular media, Phys. Rev. Lett. **130**, 098202 (2023).

[17] V. Lee, S. R. Waitukaitis, M. Z. Miskin, and H. M. Jaeger, Direct observation of particle interactions and clustering in charged granular streams, Nat. Phys. **11**, 733 (2015).

[18] See Supplemental Material at http://link.aps.org/supplemental/10.1103/PhysRevResearch.7.023017 for movies of quenching and annealing process and details about the experiment and simulation.

[19] J. R. Royer, D. J. Evans, L. Oyarte, Q. Guo, E. Kapit, M. E. Möbius, S. R. Waitukaitis, and H. M. Jaeger, High-speed tracking of rupture and clustering in freely falling granular streams, Nature (London) **459**, 1110 (2009).

[20] M. X. Lim, B. VanSaders, A. Souslov, and H. M. Jaeger, Mechanical properties of acoustically levitated granular rafts, Phys. Rev. X **12**, 021017 (2022).

[21] P. B. Muller and H. Bruus, Numerical study of thermoviscous effects in ultrasound-induced acoustic streaming in microchannels, Phys. Rev. E **90**, 043016 (2014).

[22] E. P. Lewandowski, M. J. Cavallaro, L. Botto, J. C. Bernate, V. Garbin, and K. J. Stebe, Orientation and self-assembly of cylindrical particles by anisotropic capillary interactions, Langmuir **26**, 15142 (2010).

[23] S. Ramananarivo, E. Ducrot, and J. Palacci, Activity-controlled annealing of colloidal monolayers, Nat. Commun. **10**, 3380 (2019).

[24] L. Assoud, F. Ebert, P. Keim, R. Messina, G. Maret, and H. Löwen, Ultrafast quenching of minary colloidal suspensions in an external magnetic field, Phys. Rev. Lett. **102**, 238301 (2009).

[25] Q. Chen, S. C. Bae, and S. Granick, Directed self-assembly of a colloidal kagome lattice, Nature (London) **469**, 381 (2011).